Controllable spin current in van der Waals ferromagnet Fe$_3$GeTe$_2$

Jiaqi Zhou [*] and Jean-Christophe Charlier[†]

Institute of Condensed Matter and Nanosciences (IMCN), Université catholique de Louvain, B-1348 Louvain-la-Neuve, Belgium

The control of spin current is pivotal for spintronic applications, especially for spin-orbit torque devices. The spin Hall effect is a prevalent method to generate spin current. However, it is difficult to manipulate its spin polarization in a nonmagnet. Recently, the discovery of spin current in ferromagnets offers an opportunity to realize the manipulation. In the present Letter, the spin current in the van der Waals ferromagnet Fe$_3$GeTe$_2$ (FGT) with varying magnetization is theoretically investigated. It has been observed that the spin current in FGT presents a nonlinear behavior with respect to magnetization. In-plane and out-of-plane spin polarizations emerge simultaneously, and the bilayer FGT can even exhibit arbitrary polarization owing to the reduced symmetry. More intriguingly, the correlation between the anomalous Hall effect and spin anomalous Hall effect has been interpreted from the aspect of Berry curvature and spin. This work illustrates that the interplay of magnetism and symmetry can effectively control the magnitude and polarization of the spin current, providing a practical method to realize exotic spin-orbit torques.

Introduction. Spin-orbit-coupling (SOC) effects are the frontier of spintronics and attract widespread interest. Versatile SOC effects stimulate fascinating phenomena, and improve the performances of magnetic random access memory (MRAM) [1,2]. For instance, perpendicular magnetic anisotropy (PMA) greatly increases the storage density of MRAM [3], and spin-orbit torque (SOT) can realize ultrafast switching as well as low-power writing operation [4]. The last decade has witnessed the endeavor of researchers to realize SOT switching [5]. A conventional SOT device consists of a ferromagnet/heavy metal bilayer structure, and the spin current in the heavy metal is employed to induce SOT and switch the magnetization of the ferromagnet [6,7]. Spin current can be generated by the spin Hall effect (SHE) [8]. However, due to the constraint on SHE imposed by crystal symmetry, the torque of perpendicular-flowing spin current is forced to be in plane [6]. Thus, the switching of perpendicular magnetization requires an external magnetic field, which hinders the device minimization. To solve this difficulty, various methods have been proposed, such as the assistance of spin-transfer torque [9], an asymmetric structural design [10], as well as using low-symmetry crystals as the torque sources [11–13]. More intriguingly, recent efforts have been expanded to explore the spin current in ferromagnets [14–17]. Superior to heavy metals, the magnetization in ferromagnets can break the con-

straint of symmetry, thus enabling diverse polarizations of spin current.

The spin current in ferromagnets can be attributed to the anomalous Hall effect (AHE) [18]. When the anomalous Hall current, i.e., spin-polarized current, occurs in a ferromagnet, it is naturally accompanied by a spin current. This phenomenon is called the spin anomalous Hall effect (SAHE), where the spin polarization is collinear with magnetization [15]. Several experimental and theoretical works have reported the spin current in ferromagnets. Generally, experimental works claim that the spin currents in ferromagnets completely originate from SAHE [15,19,20]. However, contradictory results appeared regarding whether the spin current is dependent on the magnetization of the ferromagnet [15–17,19–22]. Meanwhile, theoretical works also present different interpretations. It has been stated that the spin component transverse to the magnetization rapidly precesses and dephases in a ferromagnet, suggesting that the spin current only has spin along the magnetization, and its origin is SAHE exclusively [14]. However, recent first-principles simulations demonstrate that the spin current in 3d ferromagnets is composed of two contributions, SAHE and SHE. The former is dependent on the magnetization while the later is not. Moreover, the spin current with a spin component transverse to the magnetization is protected from dephasing [23,24]. Recently, a magnetization-dependent SHE was also reported in 3d ferromagnets [25]. In fact, the debate is focusing on the different definitions of SAHE and SHE. Indeed, although previous theoretical works have already provided intuitive understandings of the spin current in ferromagnets, explicit interpretations of SAHE based on the linear response theory are still missing. Besides, even if current studies are limited to conventional 3d ferromagnets, the development of van der Waals (vdW) materials provides two-dimensional (2D) ferromagnets [26,27] as ideal platforms to investigate the spin current. The representative

---

*jiaqi.zhou@uclouvain.be
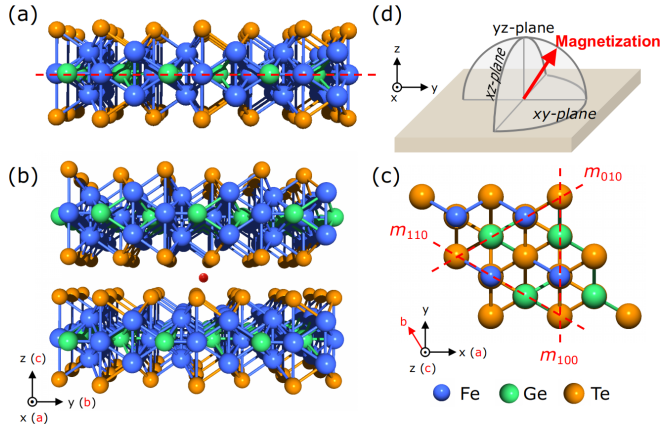†jean-christophe.charlier@uclouvain.be

FIG. 1. (a) Atomic model of monolayer FGT with a mirror symmetry (the red dashed line). (b) Atomic model of bilayer FGT with an inversion center (the red point). (c) Top view of bilayer FGT including mirror symmetries. Fe, Ge, and Te are represented by blue, green, and orange balls, respectively. (d) Illustration of the magnetization evolution in different planes.

material is metallic Fe_3GeTe_2 (FGT), which can exhibit gate-tunable room-temperature ferromagnetism [28,29]. Different from other cubic ferromagnets, FGT is a uniaxial crystal with low symmetry. More interestingly, changing the thickness can modify the structural phase of few-layer FGT, giving a broad space to investigate diverse spin current tensors.

In this Letter, the spin current in Fe_3GeTe_2 ferromagnets has been systematically investigated using *ab initio* calculations. Monolayer and bilayer FGT can exhibit nonlinear spin current with respect to magnetization, making its magnitude controllable. More intriguingly, both the magnetization and the low-symmetry structure of FGT can break the constraint on spin current tensors, enabling the simultaneous occurrence of in-plane and out-of-plane spin polarizations. Using the Kubo formula, the origin of the spin current is classified according to the spin, and the correlation between AHE and SAHE is clarified. This Letter demonstrates that the interplay of magnetism and symmetry can create an unconventional spin current, and interprets the origin of spin current in a ferromagnet.

Models and methods. The linear response tensor of an electric field is restricted by the symmetry of the crystal [30–33]. Consequently, crystals in different phases would exhibit various Hall currents [34]. FGT is a uniaxial crystal in a hexagonal structure. Even if both exhibit three mirrors orthogonal to the xy plane as shown in Fig. 1(c), the monolayer FGT crystallizes in the $P\bar{6}m2$ phase with a mirror $\mathcal{M}$ normal to the z direction [see Fig. 1(a)], while the bilayer FGT is in the $P\bar{3}m1$ phase with the spatial inversion $\mathcal{P}$ [see Fig. 1(b)]. The structural discrepancy creates an opportunity to explore various Hall currents in these two types of FGT. The intrinsic anomalous Hall conductivity (AHC) and spin Hall conductivity (SHC) have been investigated using *ab initio* calculations, as implemented in QUANTUM ESPRESSO [35] and WANNIER90 [36] (see details in the Supplemental Material [37]).

Definitions of Hall conductivities. The present work focuses on the response current along x axis when the electric field is applied along y axis. The spin polarization γ is projected onto the x, y, or z axis.

In the 2D system, the anomalous Hall conductivity can be evaluated by the Kubo formula as [38,39]

$$\sigma_{AH} = -\frac{e^2}{\hbar} \int_{BZ} \frac{d^2k}{(2\pi)^2} \Omega(\mathbf{k}), \qquad (1)$$

where BZ denotes the first Brillouin zone, $\Omega(\mathbf{k})$ is the Berry curvature (BC), as

$$\Omega(\mathbf{k}) = \sum_n f_{n\mathbf{k}} \Omega_n(\mathbf{k}), \qquad (2)$$

$$\Omega_n(\mathbf{k}) = \hbar^2 \sum_{m \neq n} \frac{-2\,\mathrm{Im}[\langle n\mathbf{k}|\hat{v}_x|m\mathbf{k}\rangle \langle m\mathbf{k}|\hat{v}_y|n\mathbf{k}\rangle]}{(\epsilon_{n\mathbf{k}} - \epsilon_{m\mathbf{k}})^2}, \qquad (3)$$

where $f_{n\mathbf{k}}$ is the Fermi-Dirac distribution function, $\epsilon_{i\mathbf{k}}$ ($i = m, n$) is the eigenvalue, and $\hat{v}_\alpha$ ($\alpha = x, y$) denotes the velocity operator.

In analogy with that of a nonmagnet [40,41], the spin Hall conductivity of the 2D ferromagnet is given as

$$\sigma_{SH,\gamma} = -\frac{e^2}{\hbar} \int_{BZ} \frac{d^2k}{(2\pi)^2} \Omega_\gamma(\mathbf{k}), \qquad (4)$$

where $\Omega_\gamma(\mathbf{k})$ is the spin Berry curvature (SBC), as

$$\Omega_\gamma(\mathbf{k}) = \sum_n f_{n\mathbf{k}} \Omega_{n,\gamma}(\mathbf{k}), \qquad (5)$$

$$\Omega_{n,\gamma}(\mathbf{k}) = \hbar^2 \sum_{m \neq n} \frac{-2\,\mathrm{Im}[\langle n\mathbf{k}|\frac{1}{2}\{\hat{\sigma}_\gamma, \hat{v}_x\}|m\mathbf{k}\rangle \langle m\mathbf{k}|\hat{v}_y|n\mathbf{k}\rangle]}{(\epsilon_{n\mathbf{k}} - \epsilon_{m\mathbf{k}})^2}, \qquad (6)$$

where $\hat{\sigma}_\gamma$ is the spin operator, and $\frac{1}{2}\{\hat{\sigma}_\gamma, \hat{v}_x\} = \frac{1}{2}(\hat{\sigma}_\gamma \hat{v}_x + \hat{v}_x \hat{\sigma}_\gamma)$.

Since both AHC and SHC occur in a ferromagnet, the correlation between them is worth investigating. First, we define a spin matrix **S** whose dimension is the number of eigenstates, and the element at the mth row and nth column is $\langle m\mathbf{k}|\hat{\sigma}_\gamma|n\mathbf{k}\rangle$. It can be seen that the nth diagonal element of **S** is the spin of the nth eigenstate, called the intraband spin. Then, through inserting a projection operator $\sum_t |t\mathbf{k}\rangle\langle t\mathbf{k}| = 1$ into Eq. (6) and considering $t = n, m$, respectively, the diagonal elements of **S**, i.e., $\langle n\mathbf{k}|\hat{\sigma}_\gamma|n\mathbf{k}\rangle$ and $\langle m\mathbf{k}|\hat{\sigma}_\gamma|m\mathbf{k}\rangle$, can be extracted. Since both $\langle n\mathbf{k}|\hat{\sigma}_\gamma|n\mathbf{k}\rangle$ and $\langle m\mathbf{k}|\hat{\sigma}_\gamma|m\mathbf{k}\rangle$ are real, this diagonal part can be denoted by $\bar{\Omega}_{n,\gamma}(\mathbf{k})$ as

$$\bar{\Omega}_{n,\gamma}(\mathbf{k}) = \hbar^2 \sum_{m \neq n} [\langle n\mathbf{k}|\hat{\sigma}_\gamma|n\mathbf{k}\rangle + \langle m\mathbf{k}|\hat{\sigma}_\gamma|m\mathbf{k}\rangle]$$
$$\times \frac{-\,\mathrm{Im}[\langle n\mathbf{k}|\hat{v}_x|m\mathbf{k}\rangle \langle m\mathbf{k}|\hat{v}_y|n\mathbf{k}\rangle]}{(\epsilon_{n\mathbf{k}} - \epsilon_{m\mathbf{k}})^2}. \qquad (7)$$

As a result of the intraband spin, Eq. (7) is called the band-resolved intraband spin Berry curvature (intra-SBC). With this quantity and its summation over the occupied bands, the intraband spin Hall conductivity (intra-SHC) is defined as

$$\bar{\Omega}_\gamma(\mathbf{k}) = \sum_n f_{n\mathbf{k}} \bar{\Omega}_{n,\gamma}(\mathbf{k}), \qquad (8)$$

$$\sigma_{SH,\gamma}^{intra} = -\frac{e^2}{\hbar} \int_{BZ} \frac{d^2k}{(2\pi)^2} \bar{\Omega}_\gamma(\mathbf{k}). \qquad (9)$$

The correlation between AHC and intra-SHC is discussed as follows. It has been reported that AHC is dominated by $\Omega(\boldsymbol{k})$ spikes at limited $\boldsymbol{k}$ points, where the spin-orbit-split bands cross the Fermi energy E_F [38,39]. These spikes are caused by the small energy gaps between the nth and the mth bands (one occupied and one unoccupied), which lead to small energy denominators [$(\epsilon_{nk} - \epsilon_{mk})^2$]. Similar to AHC, the dominant contribution to intra-SHC also comes from spikes in BZ. Moreover, at these $\boldsymbol{k}$ points, bands have analogous spin [37], indicating that around these $\bar{\Omega}_\gamma(\boldsymbol{k})$ spikes, $\langle n\boldsymbol{k}|\hat{\sigma}_\gamma|n\boldsymbol{k}\rangle \approx \langle m\boldsymbol{k}|\hat{\sigma}_\gamma|m\boldsymbol{k}\rangle$, making Eq. (7) approximated as

$$\bar{\Omega}_{n,\gamma}(\boldsymbol{k}) \approx \langle n\boldsymbol{k}|\hat{\sigma}_\gamma|n\boldsymbol{k}\rangle\hbar^2 \sum_{m \neq n} \frac{-2\,\mathrm{Im}[\langle n\boldsymbol{k}|\hat{v}_x|m\boldsymbol{k}\rangle\langle m\boldsymbol{k}|\hat{v}_y|n\boldsymbol{k}\rangle]}{(\epsilon_{nk} - \epsilon_{mk})^2}$$
$$= \langle n\boldsymbol{k}|\hat{\sigma}_\gamma|n\boldsymbol{k}\rangle\Omega_n(\boldsymbol{k}). \tag{10}$$

Equation (10) illustrates that the spin of eigenstate is the bridge to connect BC and intra-SBC. On the other hand, only considering the direction, $\hat{\mathbf{m}} = \frac{\mathbf{m}}{|\mathbf{m}|}$ is used to denote the unit vector of magnetization. This unit vector is projected onto three axes as $\hat{\mathbf{m}} = [m_x, m_y, m_z]$, and

$$m_\gamma \sim \int_{\mathrm{BZ}} \frac{d^2k}{(2\pi)^2} \sum_n f_{nk}\langle n\boldsymbol{k}|\hat{\sigma}_\gamma|n\boldsymbol{k}\rangle. \tag{11}$$

Considering Eqs. (3), (10), and (11), AHC and intra-SHC can be related by the following formula,

$$\boldsymbol{\sigma}_{\mathrm{SH}}^{\mathrm{intra}} \approx \eta\sigma_{\mathrm{AH}}\hat{\mathbf{m}}, \tag{12}$$

where $\boldsymbol{\sigma}_{\mathrm{SH}}^{\mathrm{intra}} = [\sigma_{\mathrm{SH},x}^{\mathrm{intra}}, \sigma_{\mathrm{SH},y}^{\mathrm{intra}}, \sigma_{\mathrm{SH},z}^{\mathrm{intra}}]$, and the coefficient η denotes the conversion efficiency from AHC to intra-SHC. Note that $\boldsymbol{\sigma}_{\mathrm{SH}}^{\mathrm{intra}}$, η, and σ_{AH} are not constants but varying with respect to $\hat{\mathbf{m}}$. For brevity, $\hat{\mathbf{m}}$ is omitted in the notations of these quantities. The approximation is due to $\langle n\boldsymbol{k}|\hat{\sigma}_\gamma|n\boldsymbol{k}\rangle$ not being a good quantum number, and it will be shown that this approximation is negligible in the case of Eq. (12). More significantly, $\boldsymbol{\sigma}_{\mathrm{SH}}^{\mathrm{intra}}$ can be regarded as the intrinsic SAHE, since it denotes the spin current converted from AHE, and its spin orientation is along the magnetization. In a nutshell, the explicit interpretations of SAHE are presented using the Kubo formula [Eqs. (7)–(9)], making AHE and SAHE correlated through the magnetization within the approximation $\langle n\boldsymbol{k}|\hat{\sigma}_\gamma|n\boldsymbol{k}\rangle \approx \langle m\boldsymbol{k}|\hat{\sigma}_\gamma|m\boldsymbol{k}\rangle$.

In the above section, the diagonal elements of the spin matrix have been considered in order to define intra-SHC. Meanwhile, the off-diagonal part also contributes to the spin current. Through inserting $\sum_t |t\boldsymbol{k}\rangle\langle t\boldsymbol{k}| = 1$ into Eq. (6) and considering $t \neq n, m$, respectively, the off-diagonal part, called interband spin Berry curvature (inter-SBC), is defined as

$$\tilde{\Omega}_{n,\gamma}(\boldsymbol{k}) = \hbar^2 \sum_{\substack{m \neq n \\ t \neq m,n}} -\mathrm{Im}\left[\langle n\boldsymbol{k}|\hat{\sigma}_\gamma|t\boldsymbol{k}\rangle \times \frac{\langle t\boldsymbol{k}|\hat{v}_x|m\boldsymbol{k}\rangle\langle m\boldsymbol{k}|\hat{v}_y|n\boldsymbol{k}\rangle}{(\epsilon_{nk} - \epsilon_{mk})^2}\right.$$
$$\left. + \langle t\boldsymbol{k}|\hat{\sigma}_\gamma|m\boldsymbol{k}\rangle \times \frac{\langle n\boldsymbol{k}|\hat{v}_x|t\boldsymbol{k}\rangle\langle m\boldsymbol{k}|\hat{v}_y|n\boldsymbol{k}\rangle}{(\epsilon_{nk} - \epsilon_{mk})^2}\right]. \tag{13}$$
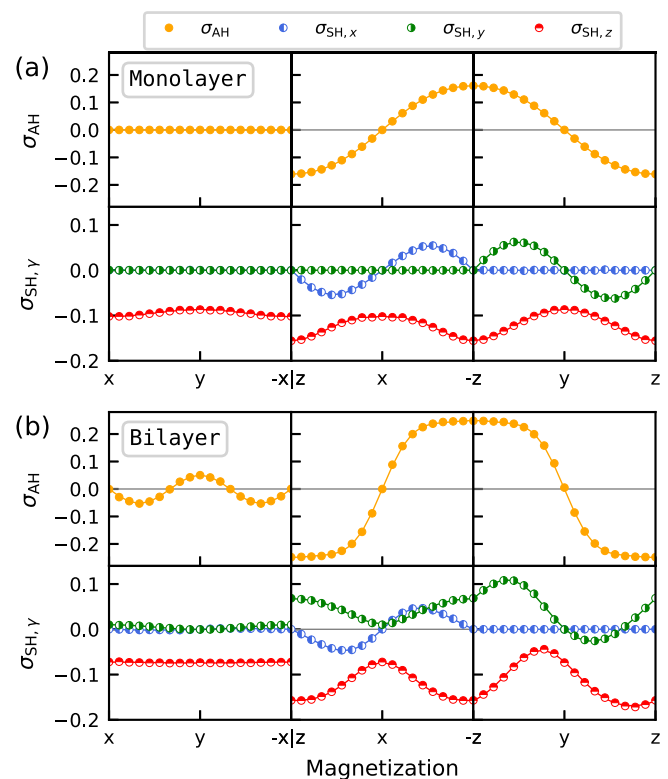

FIG. 2. AHC and SHC of (a) monolayer and (b) bilayer FGT with magnetization rotating inside xy, xz, and yz planes. σ_{AH} of xy magnetization is magnified ten times in (b). Markers denote the *ab initio* data, while lines depict the fitting curves. SHC has been multiplied by a factor of $-2e/\hbar$, thus the units of both σ_{AH} and $\sigma_{\mathrm{SH},\gamma}$ are $e^2/\hbar$.

With this quantity and its summation, the interband spin Hall conductivity (inter-SHC) is defined as

$$\tilde{\Omega}_\gamma(\boldsymbol{k}) = \sum_n f_{nk}\tilde{\Omega}_{n,\gamma}(\boldsymbol{k}), \tag{14}$$

$$\sigma_{\mathrm{SH},\gamma}^{\mathrm{inter}} = -\frac{e^2}{\hbar} \int_{\mathrm{BZ}} \frac{d^2k}{(2\pi)^2} \tilde{\Omega}_\gamma(\boldsymbol{k}). \tag{15}$$

For the sake of intelligibility, all of the terminologies and notations used above are summarized in the Supplemental Material [37].

AHC and SHC. The *ab initio* calculations have been performed to obtain AHC and SHC with rotating magnetization as depicted in Fig. 1(d), and the results at E_F are summarized in Fig. 2. Although it is conventional to set $\hat{\mathbf{m}}$ along the z axis to maximize AHC, indeed, AHC is dependent on $\hat{\mathbf{m}}$ [42]. Breaking the time-reversal symmetry ($\mathcal{T}$) [43], AHC shall be expressed by the odd-order terms with respect to magnetization. On the contrary, SHC is invariant under $\mathcal{T}$ [43] and described by even-order terms. The fitting curves of the *ab initio* data are obtained using SCIPY package [44], and the complete expressions can be found in the Supplemental Material [37].

Figure 2(a) presents the AHC and SHC of monolayer FGT. It can be observed that $\sigma_{\mathrm{AH}} = 0$ when the magnetization is in the xy plane. In contrast, both the xz- and

yz-magnetization cases allow the occurrence of AHC. When $\hat{\mathbf{m}}$ is along $-z$, the magnitude of AHC reaches the maximum, $0.134 \, e^2/\hbar$, larger than other vdW ferromagnets [45]. According to the directions of spin polarization, $\boldsymbol{\sigma}_{\mathrm{SH}}$ is decomposed into $\sigma_{\mathrm{SH},x}$, $\sigma_{\mathrm{SH},y}$, $\sigma_{\mathrm{SH},z}$. Compared with the nonmagnetic transition metal dichalcogenides [46], the monolayer FGT can exhibit much larger SHC. In addition, the SHC in FGT is nonlinear and periodic with respect to $\hat{\mathbf{m}}$, indicating the magnitude of spin current can be controlled by magnetization. More intriguingly, various spin current emerges in FGT, making this system more practical for applications. For instance, when the magnetization is in the xz plane, $\sigma_{\mathrm{SH},x}$ and $\sigma_{\mathrm{SH},z}$ appear simultaneously, making the spin current induce both in-plane and out-of-plane torques.

Different from the monolayer, the bilayer FGT, with $\mathcal{P}$ symmetry, can exhibit nonzero σ_{AH} with a period of $2\pi/3$ in the case of xy magnetization [see Fig. 2(b)]. This can be explained by Neumann's principle, which states that the symmetries of physical property must include all the symmetries of crystal [30,31,47]. Since the magnetization is a pseudovector, when $\hat{\mathbf{m}}$ is orthogonal to any mirror shown in Fig. 1(c), $\mathcal{M}$ would be preserved, thus prohibiting the occurrence of AHC. Consequently, $\sigma_{\mathrm{AH}} = 0$ occurs periodically. When $\hat{\mathbf{m}}$ points to other orientations, mirrors would be broken and not restrict AHC. In addition, compared with the monolayer, a larger AHC of $0.248 \, e^2/\hbar$ is found in the bilayer FGT. It is worth noting that more diverse SHCs are found in the bilayer FGT. In the xz-magnetization scenario, $\sigma_{\mathrm{SH},x}$, $\sigma_{\mathrm{SH},y}$, and $\sigma_{\mathrm{SH},z}$ can all occur simultaneously. The existence of $\sigma_{\mathrm{SH},y}$ in bilayer FGT is distinct from that in monolayer FGT. The reason is attributed to the difference in symmetry, i.e., the xz-magnetization monolayer preserves the $\mathcal{TC}$ ($\mathcal{C}$ denotes the rotational symmetry) while the bilayer does not, thus the latter can stimulate peculiar SHC tensor. The present findings evidently demonstrate that the interplay between magnetism and symmetry is effective to manipulate the magnitude and polarization of spin current.

Conversion from AHC to SAHC. It has been discussed that SHC can be decomposed into intra-SHC and inter-SHC, and the intra-SHC (i.e., SAHC) depends on AHC. The conversion from AHC to intra-SHC is essential to comprehend intra-SHC. Through *ab initio* calculations, the AHC and intra-SHC with xz magnetization have been investigated [see markers in Figs. 3(a) and 3(c)]—note the intra-SHC was calculated using the intra-SBC [Eqs. (7)–(9)]. Using Eq. (12), the conversion efficiency η from AHC to intra-SHC can be derived by $\sigma_{\mathrm{SH},\gamma}^{\mathrm{intra}}/(m_\gamma \sigma_{\mathrm{AH}})$, and η is displayed by markers in Fig. 3(b). Using the fitting functions of AHC and η, the evolution of intra-SHC with respect to $\hat{\mathbf{m}}$ can be obtained and plotted using Eq. (12). Figure 3(c) illustrates that in both monolayer and bilayer FGT, the curves plotted by Eq. (12) (see the bold lines) can perfectly characterize the *ab initio* data of intra-SHC for any tensor element and any magnetization direction, demonstrating that the set of conversion efficiency is universal. Moreover, the case of yz magnetization draws the same conclusion with the same η parameters [37]. Thus, the correlation between AHC and intra-SHC, i.e., Eq. (12), is verified. Indeed, the anomalous Hall current is always accompanied by spin anomalous Hall current, with a spin orientation collinear with $\hat{\mathbf{m}}$ [14]. Consequently, intra-SHC is expected
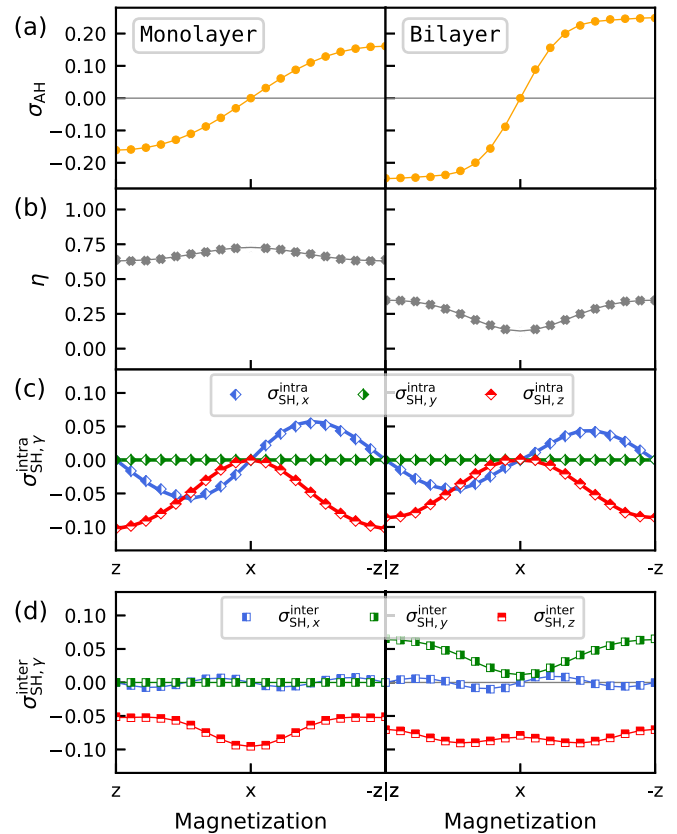

FIG. 3. (a) AHC, (b) conversion efficiency, (c) intra-SHC, and (d) inter-SHC of monolayer and bilayer FGT, respectively, with the xz magnetization. The colorful markers in (a), (c), and (d) denote the *ab initio* data, while the gray markers in (b) are derived data. (a), (b), and (d) depict the fitting curves (slim lines), while (c) depicts the curves of Eq. (12) (bold lines). The units of σ_{AH}, $\sigma_{\mathrm{SH},\gamma}^{\mathrm{intra}}$, and $\sigma_{\mathrm{SH},\gamma}^{\mathrm{inter}}$ are $e^2/\hbar$.

to be dependent on AHC. The multiplier $\hat{\mathbf{m}} = [m_x, m_y, m_z]$ can be regarded as the projection onto x, y, and z direction, producing three spin current components $\sigma_{\mathrm{SH},x}^{\mathrm{intra}}$, $\sigma_{\mathrm{SH},y}^{\mathrm{intra}}$, $\sigma_{\mathrm{SH},z}^{\mathrm{intra}}$, respectively.

Different from the intra-SHC, there is no universal conversion efficiency from AHC to inter-SHC, which is shown in Fig. 3(d). It is worth mentioning that even if the spin orientation is in the xz plane, inter-SHC can still contribute to the y polarization (nonzero $\sigma_{\mathrm{SH},y}^{\mathrm{inter}}$) in bilayer FGT, i.e., the y-polarization SHC is exclusively contributed by inter-SHC.

Berry curvatures. The band structures of bilayer FGT have been investigated to present the microscopic mechanism of the Hall conductivities. The Te-p and Fe-d orbitals make the dominant contributions to the bands around E_F [37]. The projected bands along M-K are selected to clarify the correlations of various Berry curvatures. Figure 4(a) shows that at E_F, the spin orientations are well (anti)aligned with the magnetization. Figures 4(b)–4(e) present the *ab initio* results of various Berry curvatures. It can be seen that the main contributions to Berry curvatures come from the band pairs with small energy gaps. As expected, large spikes of $\bar{\Omega}_z(\boldsymbol{k})$ only occur at limited $\boldsymbol{k}$ points such as the P point, where the bands have analogous
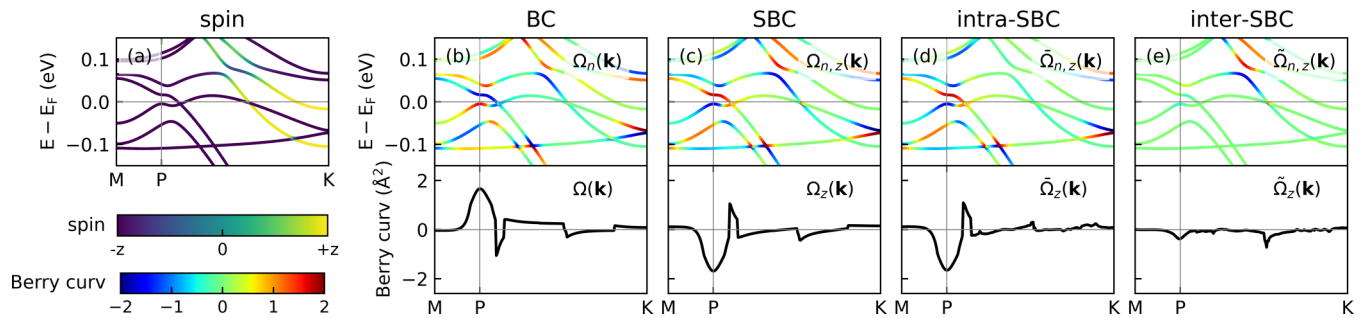
FIG. 4. (a) Spin projected bands of bilayer FGT with z magnetization, where the dark (bright) color denotes spin along $-z$ ($+z$). (b) BC, (c) SBC, (d) intra-SBC, and (e) inter-SBC. The upper panels show the bands projected by different Berry curvatures, and the lower panels depict the summation results. All the Berry curvatures are in log scale [Eq. (S9)], where the blue (red) color denotes the negative (positive) curvature value. E_F is set to zero.

spin. This phenomenon can be interpreted by Eq. (7), which shows that $\bar{\Omega}_z(\mathbf{k})$ is proportional to the summation of spin expectation values. On the contrary, $\tilde{\Omega}_z(\mathbf{k})$ is mainly contributed by the bands with misaligned spin away from E_F.

The conversion from AHC to intra-SHC has been studied from the conductivity aspect in Fig. 3. To reveal the microscopic mechanisms, the conversion from BC to intra-SBC would be discussed at two levels: (i) the band-resolved conversion efficiency $\eta_n(\mathbf{k}) = \bar{\Omega}_{n,z}(\mathbf{k})/\Omega_n(\mathbf{k})$, and (ii) the summation result $\eta(\mathbf{k}) = \bar{\Omega}_z(\mathbf{k})/\Omega(\mathbf{k})$. Figures 4(a), 4(b) and 4(d) demonstrate that $\eta_n(\mathbf{k})$ is determined by the spin of eigenstate, making $\eta_n(\mathbf{k}) = \langle n\mathbf{k}|\hat{\sigma}_z|n\mathbf{k}\rangle = \pm 1$ when the spin is collinear with the magnetization. For instance, two bands around E_F (one occupied and one unoccupied) at the P point have spin along $-z$, i.e., $\eta_n(\mathbf{k}) = -1$, leading to the opposite signs of $\Omega_n(\mathbf{k})$ and $\bar{\Omega}_{n,z}(\mathbf{k})$ on these two bands, as shown in the upper panels of Figs. 4(b) and 4(d). On the other hand, although $\Omega(\mathbf{k})$ [$\bar{\Omega}_z(\mathbf{k})$] is a property of the occupied manifold, it is mostly determined by the band structure near the Fermi surface, since the contributions of the bands far away from E_F are canceled by each other [48,49]. Consequently, $\eta(\mathbf{k})$, to some extent, is determined by the spin of the occupied state around E_F. For instance, at the P point, the last occupied band exhibits spin along $-z$, resulting in $\eta(\mathbf{k}) = -1$ as shown in the lower panels of Figs. 4(b) and 4(d). Note that the conductivities σ_{AH} and $\sigma_{\mathrm{SH},z}^{\mathrm{intra}}$ are, respectively, the integral of $\Omega(\mathbf{k})$ and $\bar{\Omega}_z(\mathbf{k})$ with respect to $\mathbf{k}$. However, it should be emphasized that η is not the integral of $\eta(\mathbf{k})$ with respect to $\mathbf{k}$, since neither $\Omega(\mathbf{k})$, $\bar{\Omega}_z(\mathbf{k})$, nor $\eta(\mathbf{k})$ is a constant in the Brillouin zone of FGT. In fact, there is no simple relation between the global conversion efficiency η and the microscopic $\eta_n(\mathbf{k})$ in the FGT system. Thus, the global η shall be obtained using the global conductivities AHC and intra-SHC, and the value of η is not restricted in the range of $[-1, 1]$.

Effective model. An effective $k \cdot p$ model is constructed to reveal more physical principles. Under the basis of $[c_{1,k\uparrow}, c_{2,k\uparrow}, c_{1,k\downarrow}, c_{2,k\downarrow}]^T$ where 1 and 2 denote the orbital index, the 4×4 Hamiltonian can be expressed as

$$H = (mk^2 + \delta)\tau_z + \alpha k_x \sigma_z \otimes \tau_x + \beta k_y \sigma_0 \otimes \tau_y + M\sigma_z \otimes \tau_0,$$

(16)

where σ_i and τ_i are Pauli matrices for the spin and orbital degrees of freedom, respectively. m denotes the effective mass, and δ is the strength of band inversion. The α and β terms respectively denote the SOC and the orbital hybridization. The last term indicates a magnetic field along the z direction. This model qualitatively characterizes the *ab initio* bands around the P point and E_F shown in Fig. 4, as well as the properties of spin and Berry curvatures. Moreover, it reveals that both Ω_n and $\bar{\Omega}_{n,z}$ are proportional to the strength of the orbital hybridization while inversely proportional to SOC and band inversion [37].

Summary. The origin and control of spin current in both monolayer and bilayer Fe$_3$GeTe$_2$ have been systematically investigated. It exhibits nonlinear behavior with respect to magnetization, as well as the simultaneous occurrence of in-plane and out-of-plane spin polarizations. Superior to the monolayer case, bilayer Fe$_3$GeTe$_2$ can present unusual arbitrary spin current element due to the reduced symmetry. Using the concepts of Berry curvature and intraband spin Berry curvature, the correlation between anomalous Hall effect and spin anomalous Hall effect has been clarified, as well as the corresponding conversion efficiency. An effective $k \cdot p$ model illustrates that the orbital hybridization is essential for Berry curvatures. The present research demonstrates that the interplay between magnetism and symmetry can control both the magnitude and polarization of spin current, further stimulating exotic spin-orbit torques for spintronic devices.

[1] B. Dieny, I. L. Prejbeanu, K. Garello, P. Gambardella, P. Freitas, R. Lehndorff, W. Raberg, U. Ebels, S. O. Demokritov, J. Akerman, A. Deac, P. Pirro, C. Adelmann, A. Anane, A. V. Chumak, A. Hirohata, S. Mangin, S. O. Valenzuela, M. C. Onbaşlı, M. D'Aquino *et al.*, Opportunities and challenges for spintronics in the microelectronics industry, Nat. Electron. **3**, 446 (2020).

[2] S. Peng, D. Zhu, J. Zhou, B. Zhang, A. Cao, M. Wang, W. Cai, K. Cao, and W. Zhao, Modulation of heavy metal/ferromagnetic metal interface for high-performance spintronic devices, Adv. Electron. Mater. **5**, 1900134 (2019).

[3] S. Ikeda, K. Miura, H. Yamamoto, K. Mizunuma, H. D. Gan, M. Endo, S. Kanai, J. Hayakawa, F. Matsukura, and H. Ohno, A perpendicular-anisotropy CoFeB-MgO magnetic tunnel junction, Nat. Mater. **9**, 721 (2010).

[4] R. Ramaswamy, J. M. Lee, K. Cai, and H. Yang, Recent advances in spin-orbit torques: Moving towards device applications, Appl. Phys. Rev. **5**, 031107 (2018).

[5] A. Manchon, J. Železný, I. M. Miron, T. Jungwirth, J. Sinova, A. Thiaville, K. Garello, and P. Gambardella, Current-induced spin-orbit torques in ferromagnetic and antiferromagnetic systems, Rev. Mod. Phys. **91**, 035004 (2019).

[6] L. Liu, O. J. Lee, T. J. Gudmundsen, D. C. Ralph, and R. A. Buhrman, Current-Induced Switching of Perpendicularly Magnetized Magnetic Layers Using Spin Torque from the Spin Hall Effect, Phys. Rev. Lett. **109**, 096602 (2012).

[7] L. Zhu, D. C. Ralph, and R. A. Buhrman, Spin-Orbit Torques in Heavy-Metal-Ferromagnet Bilayers with Varying Strengths of Interfacial Spin-Orbit Coupling, Phys. Rev. Lett. **122**, 077201 (2019).

[8] J. Sinova, S. O. Valenzuela, J. Wunderlich, C. H. Back, and T. Jungwirth, Spin Hall effects, Rev. Mod. Phys. **87**, 1213 (2015).

[9] M. Wang, W. Cai, D. Zhu, Z. Wang, J. Kan, Z. Zhao, K. Cao, Z. Wang, Y. Zhang, T. Zhang, C. Park, J.-P. Wang, A. Fert, and W. Zhao, Field-free switching of a perpendicular magnetic tunnel junction through the interplay of spin-orbit and spin-transfer torques, Nat. Electron. **1**, 582 (2018).

[10] G. Yu, P. Upadhyaya, Y. Fan, J. G. Alzate, W. Jiang, K. L. Wong, S. Takei, S. A. Bender, L.-T. Chang, Y. Jiang, M. Lang, J. Tang, Y. Wang, Y. Tserkovnyak, P. K. Amiri, and K. L. Wang, Switching of perpendicular magnetization by spin-orbit torques in the absence of external magnetic fields, Nat. Nanotechnol. **9**, 548 (2014).

[11] L. Liu, C. Zhou, X. Shu, C. Li, T. Zhao, W. Lin, J. Deng, Q. Xie, S. Chen, J. Zhou, R. Guo, H. Wang, J. Yu, S. Shi, P. Yang, S. Pennycook, A. Manchon, and J. Chen, Symmetry-dependent field-free switching of perpendicular magnetization, Nat. Nanotechnol. **16**, 277 (2021).

[12] D. MacNeill, G. M. Stiehl, M. H. D. Guimaraes, R. A. Buhrman, J. Park, and D. C. Ralph, Control of spin-orbit torques through crystal symmetry in WTe₂/ferromagnet bilayers, Nat. Phys. **13**, 300 (2017).

[13] J. H. Garcia, M. Vila, C.-H. Hsu, X. Waintal, V. M. Pereira, and S. Roche, Canted Persistent Spin Texture and Quantum Spin Hall Effect in WTe₂, Phys. Rev. Lett. **125**, 256603 (2020).

[14] T. Taniguchi, J. Grollier, and M. D. Stiles, Spin-Transfer Torques Generated by the Anomalous Hall Effect and Anisotropic Magnetoresistance, Phys. Rev. Applied **3**, 044001 (2015).

[15] Y. Koike, S. Iihama, and S. Mizukami, Composition dependence of the spin-anomalous Hall effect in a ferromagnetic Fe-Co alloy, Jpn. J. Appl. Phys. **59**, 090907 (2020).

[16] S. Varotto, M. Cosset-Chéneau, C. Grèzes, Y. Fu, P. Warin, A. Brenac, J.F. Jacquot, S. Gambarelli, C. Rinaldi, V. Baltz, J.-P. Attané, L. Vila, and P. Noël, Independence of the Inverse Spin Hall Effect with the Magnetic Phase in Thin NiCu Films, Phys. Rev. Lett. **125**, 267204 (2020).

[17] J. Cramer, A. Ross, S. Jaiswal, L. Baldrati, R. Lebrun, and M. Kläui, Orientation-dependent direct and inverse spin Hall effects in Co₆₀Fe₂₀B₂₀, Phys. Rev. B **99**, 104414 (2019).

[18] N. Nagaosa, J. Sinova, S. Onoda, A. H. MacDonald, and N. P. Ong, Anomalous Hall effect, Rev. Mod. Phys. **82**, 1539 (2010).

[19] Y. Omori, E. Sagasta, Y. Niimi, M. Gradhand, L. E. Hueso, F. Casanova, and Y. C. Otani, Relation between spin Hall effect and anomalous Hall effect in 3*d* ferromagnetic metals, Phys. Rev. B **99**, 014403 (2019).

[20] S. Iihama, T. Taniguchi, K. Yakushiji, A. Fukushima, Y. Shiota, S. Tsunegi, R. Hiramatsu, S. Yuasa, Y. Suzuki, and H. Kubota, Spin-transfer torque induced by the spin anomalous Hall effect, Nat. Electron. **1**, 120 (2018).

[21] T. Seki, S. Iihama, T. Taniguchi, and K. Takanashi, Large spin anomalous Hall effect in *L*1₀-FePt: Symmetry and magnetization switching, Phys. Rev. B **100**, 144427 (2019).

[22] T. C. Chuang, D. Qu, S. Y. Huang, and S. F. Lee, Magnetization-dependent spin Hall effect in a perpendicular magnetized film, Phys. Rev. Research **2**, 032053(R) (2020).

[23] V. P. Amin, J. Li, M. D. Stiles, and P. M. Haney, Intrinsic spin currents in ferromagnets, Phys. Rev. B **99**, 220405(R) (2019).

[24] A. Davidson, V. P. Amin, W. S. Aljuaid, P. M. Haney, and X. Fan, Perspectives of electrically generated spin currents in ferromagnetic materials, Phys. Lett. A **384**, 126228 (2020).

[25] G. Qu, K. Nakamura, and M. Hayashi, Magnetization direction dependent spin Hall effect in 3*d* ferromagnets, Phys. Rev. B **102**, 144440 (2020).

[26] K. S. Burch, D. Mandrus, and J.-G. Park, Magnetism in two-dimensional van der Waals materials, Nature (London) **563**, 47 (2018).

[27] X. Lin, W. Yang, K. L. Wang, and W. Zhao, Two-dimensional spintronics for low-power electronics, Nat. Electron. **2**, 274 (2019).

[28] Z. Fei, B. Huang, P. Malinowski, W. Wang, T. Song, J. Sanchez, W. Yao, D. Xiao, X. Zhu, A. F. May, W. Wu, D. H. Cobden, J.-H. Chu, and X. Xu, Two-dimensional itinerant ferromagnetism in atomically thin Fe₃GeTe₂, Nat. Mater. **17**, 778 (2018).

[29] Y. Deng, Y. Yu, Y. Song, J. Zhang, N. Z. Wang, Z. Sun, Y. Yi, Y. Z. Wu, S. Wu, J. Zhu, J. Wang, X. H. Chen, and Y. Zhang, Gate-tunable room-temperature ferromagnetism in two-dimensional Fe₃GeTe₂, Nature (London) **563**, 94 (2018).

[30] R. E. Newnham, *Properties of Materials: Anisotropy, Symmetry, Structure* (Oxford University Press, Oxford, UK, 2005).

[31] S. V. Gallego, J. Etxebarria, L. Elcoro, E. S. Tasci, and J. M. Perez-Mato, Automatic calculation of symmetry-adapted tensors in magnetic and non-magnetic materials: A new tool of the Bilbao Crystallographic Server, Acta Crystallogr., Sect. A **75**, 438 (2019).

[32] M. Seemann, D. Ködderitzsch, S. Wimmer, and H. Ebert, Symmetry-imposed shape of linear response tensors, Phys. Rev. B **92**, 155138 (2015).

[33] F. Freimuth, S. Blügel, and Y. Mokrousov, Spin-orbit torques in strained PtMnSb from first principles, Phys. Rev. B **103**, 224414 (2021).

[34] F. Freimuth, S. Blügel, and Y. Mokrousov, Anisotropic Spin Hall Effect from First Principles, Phys. Rev. Lett. **105**, 246602 (2010).

[35] P. Giannozzi, O. Andreussi, T. Brumme, O. Bunau, M. B. Nardelli, M. Calandra, R. Car, C. Cavazzoni, D. Ceresoli, M. Cococcioni, N. Colonna, I. Carnimeo, A. D. Corso, S. de Gironcoli, P. Delugas, R. A. DiStasio, A. Ferretti, A. Floris, G. Fratesi, G. Fugallo *et al.*, Advanced capabilities for materials modelling with Quantum ESPRESSO, J. Phys.: Condens. Matter **29**, 465901 (2017).

[36] G. Pizzi, V. Vitale, R. Arita, S. Blügel, F. Freimuth, G. Géranton, M. Gibertini, D. Gresch, C. Johnson, T. Koretsune, J. Ibañez-Azpiroz, H. Lee, J.-M. Lihm, D. Marchand, A. Marrazzo, Y. Mokrousov, J. I. Mustafa, Y. Nohara, Y. Nomura, L. Paulatto *et al.*, Wannier90 as a community code: new features and applications, J. Phys.: Condens. Matter **32**, 165902 (2020).

[37] See Supplemental Material at http://link.aps.org/supplemental/10.1103/PhysRevResearch.3.L042033 for the calculation method, analytic derivations, terminologies, expressions, the *yz*-magnetization case, bands, Berry curvatures, and results of model.

[38] Y. Yao, L. Kleinman, A. H. MacDonald, J. Sinova, T. Jungwirth, D.-s. Wang, E. Wang, and Q. Niu, First Principles Calculation of Anomalous Hall Conductivity in Ferromagnetic bcc Fe, Phys. Rev. Lett. **92**, 037204 (2004).

[39] X. Wang, J. R. Yates, I. Souza, and D. Vanderbilt, *Ab initio* calculation of the anomalous Hall conductivity by Wannier interpolation, Phys. Rev. B **74**, 195118 (2006).

[40] J. Qiao, J. Zhou, Z. Yuan, and W. Zhao, Calculation of intrinsic spin Hall conductivity by Wannier interpolation, Phys. Rev. B **98**, 214402 (2018).

[41] J. Zhou, J. Qiao, A. Bournel, and W. Zhao, Intrinsic spin Hall conductivity of the semimetals MoTe$_2$ and WTe$_2$, Phys. Rev. B **99**, 060408(R) (2019).

[42] E. Roman, Y. Mokrousov, and I. Souza, Orientation Dependence of the Intrinsic Anomalous Hall Effect in hcp Cobalt, Phys. Rev. Lett. **103**, 097203 (2009).

[43] R. R. Birss, *Symmetry and Magnetism* (North-Holland, Amsterdam, 1964).

[44] SciPy, https://www.scipy.org/.

[45] X. Yang, X. Zhou, W. Feng, and Y. Yao, Tunable magneto-optical effect, anomalous Hall effect, and anomalous Nernst effect in the two-dimensional room-temperature ferromagnet 1T-CrTe$_2$, Phys. Rev. B **103**, 024436 (2021).

[46] W. Feng, Y. Yao, W. Zhu, J. Zhou, W. Yao, and D. Xiao, Intrinsic spin Hall effect in monolayers of group-VI dichalcogenides: A first-principles study, Phys. Rev. B **86**, 165108 (2012).

[47] X. Zhou, J.-P. Hanke, W. Feng, F. Li, G.-Y. Guo, Y. Yao, S. Blügel, and Y. Mokrousov, Spin-order dependent anomalous Hall effect and magneto-optical effect in the noncollinear antiferromagnets Mn$_3$$X$N with X = Ga, Zn, Ag, or Ni, Phys. Rev. B **99**, 104428 (2019).

[48] X. Wang, D. Vanderbilt, J. R. Yates, and I. Souza, Fermi-surface calculation of the anomalous Hall conductivity, Phys. Rev. B **76**, 195109 (2007).

[49] G. Y. Guo, S. Murakami, T.-W. Chen, and N. Nagaosa, Intrinsic Spin Hall Effect in Platinum: First-Principles Calculations, Phys. Rev. Lett. **100**, 096401 (2008).